Induced ferromagnetism in Mn_3N_2 phase embedded in Mn/Si_3N_4 multilayers

E. Céspedes,[1] E. Román,[1] Y. Huttel,[1] J. Chaboy,[2] J. García-López,[3] A. de Andrés,[1] and C. Prieto[1,a)]

[1]*Instituto de Ciencia de Materiales de Madrid, Consejo Superior de Investigaciones Científicas, Cantoblanco, 28049 Madrid, Spain*
[2]*Dep. de Física de la Materia Condensada and Instituto de Ciencia de Materiales de Aragón, CSIC-Universidad de Zaragoza, 50009 Zaragoza, Spain*
[3]*Centro Nacional de Aceleradores, Parque Tecnológico Cartuja'93, 41092 Sevilla, Spain*

(Received 20 April 2009; accepted 12 July 2009; published online 26 August 2009)

Room temperature ferromagnetism has been obtained for different sets of Mn/Si_3N_4 multilayers prepared by sputtering. In order to find the most suitable conditions to stabilize the ferromagnetic ordering in this system, the evolution of the magnetic properties has been studied for films in which the Si_3N_4 layer thickness was maintained constant while that of the Mn layer was varied, $[Mn(t_m)/Si_3N_4(3.4\ \text{nm})]_n$, and conversely, in $[Mn(0.7\ \text{nm})/Si_3N_4(t_{sn})]_{43}$ samples, in which the Mn layer thickness was kept constant while varying the Si_3N_4 layer thickness. Structural, compositional, electronic and magnetic characterizations have been performed by means of x-ray reflectometry, Rutherford backscattering spectrometry, x-ray photoemission spectroscopy, x-ray absorption, and superconducting quantum interference device for further knowledge of the magnetic-structural relationship in this system. Our results show that the peculiar magnetic behavior of these films is mainly related to the stabilization of a slightly distorted Mn_3N_2 phase that is induced by the Si_3N_4 at the interfaces. For samples with larger Mn layer thickness, metallic Mn and Mn_3N_2 phases coexist, which leads to a reduction of the total magnetization per Mn atom due to the presence of metallic Mn. For small Mn layer thickness ($t_m < 0.86$ nm), where noncontinuous Mn_3N_2 layers are formed, the magnetization decreases noticeably due to the superparamagnetic size limit. It has been found that the best conditions for the stabilization of the ferromagnetism in this system occur when both, the manganese-rich and the silicon nitride layers, are continuous and with similar thickness, close to 3.5 nm. © *2009 American Institute of Physics*. [DOI: 10.1063/1.3203997]

I. INTRODUCTION

Manganese nitrides have gained attention among the 3*d* transition metal nitrides for their variety of electronic and magnetic properties which are suitable for potential applications.[1–3] Recently, these materials have also generated interest in the field of diluted magnetic semiconductors (DMS) as potential magnetic secondary phases within films of Mn-doped III-V semiconductors such as Mn:GaN, Mn:GaAs, or MnInN.[4–6]

Manganese nitrides form a variety of stoichiometric phases ($\varepsilon, \zeta, \eta, \theta$) exhibiting different magnetic properties.[7] The most N rich phase, mononitride θ-MnN, has a tetragonally distorted rocksalt (NaCl) structure with an antiferromagnetic (AF) ground state.[8] It usually contains a considerable amount of N vacancies and is often labeled as Mn_6N_{5+x}. The closely related η-Mn_3N_2 phase also exhibits the NaCl structure but with an ordered array of N vacancies.[8,9] The Mn_5N_2 and Mn_2N ζ-phases have hexagonal closed packed arrangements and present, respectively, ferromagnetic (FM) and AF order.[10] Finally, the ε-Mn_4N phase consists basically in a Mn face-centered cubic structure with an interstitial N and exhibits ferrimagnetism with a curie temperature (T_C) as high as 745 K.[11]

These MnN_x phases are currently related to inhomogeneities in ternary nitride-based alloys as the possible origin of the observed ferromagnetism. Recent studies have pointed toward Mn_4N as a segregation phase showing the FM behaviors in Mn:GaN films.[5] Special attention has also been focused on the θ-MnN phase, since possible inclusions or MnN-rich regions in the matrix can have the same crystallographic structure as the semiconductor host. Although MnN has an AF ground state, it has been theoretically shown that FM order can be established depending on the MnN polymorph and the lattice parameters.[6] Band-structure calculations have been performed considering MnN in the hypothetical zinc-blende and wurtzite structures in order to get a better comprehension of these ternary nitride-based DMS systems.[6,12] Ferromagnetism with T_C of 354 K due to Mn-rich precipitates in the zinc-blende phase has been recently predicted in Mn:GaN by using the mean-field approximation.[4] Spin-density-functional theory has been used to study GaN/MnN heterostructures composed by a thin layer of biaxially strained wurtzite (w) MnN intercalated with GaN layers as a new way to obtain FM wide-gap nitride systems for spintronic applications.[13] FM order in this w-MnN on GaN has been predicted on the bases of structural relaxation at the GaN–MnN interface.

Despite all these exciting properties, up to date, there have not been reported experimental efforts to obtain FM

a)Electronic mail: cprieto@icmm.csic.es.

semiconductor/manganese nitride heterostructures. Even the interesting magnetic properties of MnN_x films have been hardly experimentally studied, probably due to difficulties in sample preparation. Just a few attempts of fabrication of MnN by reactive sputtering[10] and ion-assisted deposition,[2] Mn_3N_2 using reactive sputtering[3] and molecular beam epitaxy[1] and Mn_4N, also by reactive sputtering,[3,14] have been reported.

Very recently, the magnetic properties of the Mn/Si_3N_4 system were experimentally studied prompted by the similarities with Mn/GaN, since silicon nitride also has a wideband-gap semiconducting behavior and can be a very stable host material with high dopant concentrations.[15,16] We have reported, for the first time, ferromagnetism above room temperature (RT) in Mn/Si_3N_4 multilayered films.[17] The structural and electronic properties of few samples were studied by x-ray absorption spectroscopy (XAS) and x-ray magnetic circular dichroism, indicating the presence of a distorted noncentrosymmetric Mn_3N_2 phase with slightly shorter Mn–N distances, which was proposed to be the origin of the ferromagnetism in this system.

Here we present an extensive experimental study aimed at getting a better comprehension of the magnetic-structural relationship in the Mn/Si_3N_4 system. We have grown by sputtering different sets of Mn/Si_3N_4 films under similar experimental conditions as the previously reported ones. Different samples were prepared by varying the $Mn:Si_3N_4$ relative ratio. Evolution of the magnetic properties was studied for multilayered films with formula $[Mn(t_m)/Si_3N_4(3.4\ nm)]_n$, being t_m the Mn layer thickness and n the number of bilayers, as well as for several films labeled as $[Mn(0.7\ nm)/Si_3N_4(t_{sn})]_{43}$, being t_{sn} the Si_3N_4 layer thickness, in order to find the most suitable conditions to stabilize the FM ordering in this system.

II. EXPERIMENTAL AND COMPUTATIONAL METHODS

Mn/Si_3N_4 multilayered samples were prepared by sequential sputtering of Si_3N_4 and Mn on Si(100) substrates at RT. Si_3N_4 layers were deposited by reactive rf-sputtering from a pure Si target (99.999%) with N_2 as reactive sputtering gas.[18] The deposition rate was 2 nm/min for a rf power of 100 W. The residual pressure in the vacuum system was within the 1×10^{-7} mbar range. Mn was grown by dc-sputtering from a Mn target (99.95%) with Ar as sputtering gas and a deposition rate of ~4 nm/min for a dc power of ~10 W.

Samples with nominal formula $[Mn(t_m)/Si_3N_4(3\ nm)]_n$ and $[Mn(0.6\ nm)/Si_3N_4(t_{sn})]_{43}$ were prepared. For the first set of samples, the Si_3N_4 layer thickness was maintained constant, while the thickness of the Mn layer (t_m) was modified between 6 and 0.1 nm. In order to maintain the total amount of Mn constant, the number of bilayers (n) was progressively increased, from 5 to 75, as the Mn layer thickness was reduced. In the case of the $[Mn(0.6\ nm)/Si_3N_4(t_{sn})]_{43}$ samples, the Mn layer thickness was kept constant, while the Si_3N_4 layer thickness (t_{sn}) was varied from 6 to 0.7 nm. In this last case, the number of bilayers was always the same ($n=43$). For the two sets of multilayers, the growth process started with Si_3N_4 layer and terminated by depositing an additional 3 nm Si_3N_4 layer on top.

X-ray reflectivity (XRR) measurements were performed by using a Bruker D-8 diffractometer working with the Cu $K\alpha$ wavelength. Rutherford backscattering spectroscopy (RBS) and nuclear reaction analysis (NRA) were carried out at the Centro Nacional de Aceleradores (Sevilla, Spain). For the RBS experiments, a 2 MeV He^{2+} beam was employed, with beam diameter ~1 mm and scattering angle of 165°. The NRA measurements were done using the $^{14}N(d,\alpha_1)^{12}C$ nuclear reaction with a 1.4 MeV D^+ beam and a detection angle of 150°. A 13 μm thick Mylar foil was placed in front of the detector in order to stop the backscattered deuterons to avoid saturation of the electronic setup. For absolute N quantification of our samples, we have used as standard a 100 nm thick Si_3N_4 film grown on Si substrate. Magnetic characterization was performed by using a commercial superconducting quantum interference device magnetometer (Quantum Design MPMS-5S) in the temperature range from 5 to 400 K.

X-ray photoemission spectroscopy (XPS) measurements were performed in an ultrahigh-vacuum chamber with a base pressure of 1×10^{-10} mbar. The angle between the hemispherical analyzer (Specs-PHOIBOS100) and the plane of the surface was kept at 60° and the x-ray radiation was the Mg $K\alpha$ line (1253.6 eV). XPS spectra were recorded at the core levels of the elements present in the samples (Mn, Si, N); in the case of Mn, Mn 3p spectra were recorded with a photon energy step of 0.1 eV and a pass energy of 15 eV in order to optimize the energy resolution for further fitting analysis and Mn species identification. Prior to the data analysis, the contributions of the Mg $K\alpha$ satellite lines were subtracted and the spectra were subjected to a Shirley background subtraction formalism. The binding energy scale was calibrated with respect to the Si peak at 101.6 eV. Fittings were carried out using Gaussian–Lorentzian doublets. Within the experimental conditions, the sensitivity to the surface is rather limited and it can be assumed that the XPS spectra give information of the electronic structure that corresponds to the bulk.

X-ray absorption experiments were carried out at the BM26 and BM8 beamlines of the European Synchrotron Radiation Facility (ESRF) in Grenoble. Samples were measured in fluorescence and total electron yield (TEY) modes, respectively. No appreciable differences were found between the two detection modes and spectra are included here without distinction. The storage ring was operated with an average current of 200 mA and an electron beam energy of 6 GeV. The fixed-exit double-crystal monochromator was equipped with a pair of Si-(111) crystals being the energy resolution $\Delta E/E\sim7\times10^{-5}$ at the Mn K-edge (6539 eV). The harmonics rejection was achieved by detuning the second crystal from the parallel alignment to 70% intensity. In all cases the onset energy of the absorption process was chosen to be the maximum of the first derivative in the edge region of the absorption spectrum. The experimental x-ray absorption near edge structure (XANES) spectra were normalized after background subtraction.

Extended x-ray absorption fine structure (EXAFS) analysis was performed by using the VIPER software.[19] Oscillations were obtained after removing the background by a cubic spline polynomial fitting and EXAFS signal $\chi(k)$ was obtained by normalizing the magnitude of the oscillations to the edge jump. The corresponding pseudoradial distribution function around Mn atoms was obtained by weighting the EXAFS signals by the square wave number $\chi(k)\cdot k^2$ multiplying by a Hanning window and Fourier transform (FT). For comparison, the FT of EXAFS signal was performed within the same k-range. Theoretical EXAFS signals were generated by using the amplitude and phase backscattering functions obtained using the FEFF6 code.[20] The calculation of the EXAFS spectra was performed in a single scattering approach. The scattering potentials were obtained within the standard muffin-tin (MT) approximation and by using the nonoverlapping MT sphere approximation. The potential also includes the Hedin–Lundqvist (HL) self-energy with the Quinn correction to account for low energy electron-hole losses. Standard fits of EXAFS parameters were performed by minimizing the difference between filtered data and simulated signal where no constrains were imposed.

The computation of the Mn K-edge XANES spectra was carried out using the multiple-scattering code CONTINUUM (Ref. 21) based on the one-electron full-multiple-scattering theory.[22,23] For a complete discussion of the XANES simulation procedure we refer the reader to Refs. 24 and 25. The potential for the different atomic clusters was approximated by a set of spherically averaged MT potentials built by following the standard Mattheis' prescription.[26] The MT radii were determined following the Norman's criterion.[27] The Coulomb part of each atomic potential was generated using charge densities obtained from a nonlocal selfconsistent Dirac–Fock code.[28] The atomic orbitals were chosen to be neutral for the ground state potential, whereas different choices were used to build the final state potential and we have found during the present calculations that the screened and relaxed $Z+1$ option[29] lead to the best results for the simulation of the experimental absorption spectra at the Mn K-edge. The calculated theoretical spectra have been further convoluted with a Lorentzian shape function to account for the core-hole lifetime[30] ($\Gamma=1.2$ eV) and the experimental resolution ($\Gamma=1$ eV).

III. RESULTS AND DISCUSSION

A. XRR and RBS

XRR spectra of the studied multilayers are shown in Fig. 1 for both samples series prepared with different Mn-layer thickness (t_m) [Fig. 1(a)] and with variable Si_3N_4 layer thickness (t_{sn}) [Fig. 1(b)]. Well-defined peaks of heterostructure periodicity in the out-of-plane direction can be observed in the spectra from samples with larger t_m and t_{sn} thicknesses, while these periodicity features become smoother as t_m and t_{sn} are reduced. In fact, noncontinuous Mn layers are expected for very small t_m values, where Mn layer thickness and interface roughness become comparable. It should be noted in the figure that samples with a large bilayer number, as for instance 75 bilayers, have a total thickness too large to exhibit the short oscillations corresponding to finite size film interferences. For several samples, multilayer periodicity has been additionally confirmed by transmission electron microscopy studies.[17] Sample description and microstructural features such as average bilayer thickness are summarized in Tables I and II for samples with variable t_m and t_{sn}, respectively. Measured layer thickness is approximately 15% higher than nominal. From now on, samples are named by their experimental thickness obtained by XRR.

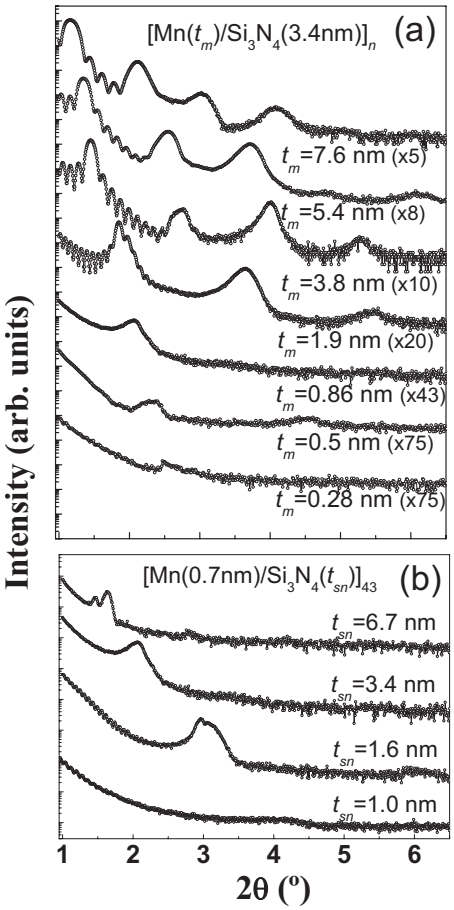

FIG. 1. (a) XRR spectra of some of the multilayered samples with different Mn-layer thickness (t_m). Experimental t_m values are shown in the figure. (b) XRR spectra of the prepared samples with different Si_3N_4-layer thickness (t_{sn}). Experimental t_m values are shown in the figure. All spectra have been vertically shifted for clearness.

In order to obtain the manganese atomic density in Mn-rich layers, the total amount of Mn has been determined by RBS. Figures 2(a) and 2(b) display spectra obtained using incident ions of 2 MeV and their corresponding simulations using the SIMNRA software package. The calculated Mn atomic density and film atomic composition obtained jointly by RBS and NRA for some representative samples are summarized in Tables I and II. Finally, a comparison between the experimental manganese layer thickness values obtained from XRR spectra and the ones calculated from RBS data considering pure metal manganese density is shown in Fig. 2(c). The obtained difference means that, even if pure Mn was sputtered, layers do not consist on metallic Mn, since to obtain the actual thickness (given by the XRR data) a smaller Mn density should be considered in calculations from RBS. On the other hand, no appreciable oxygen amount was de-

TABLE I. Description of selected samples, nominally named $[Mn(t_m)/Si_3N_4(3\ nm)]_n$: nominal Mn thickness ($t_m$), number of bilayers ($n$), nominal bilayer thickness (Λ), XRR-obtained bilayer thickness (XRR-Λ), XRR-obtained Mn thickness (XRR-t_m) and atomic composition, obtained from simulation of RBS and NRA.

Nominal t_m (nm)	n	Nominal Λ (nm)	XRR-Λ (nm)	Mn-layer atomic density (at./cm^2)	XRR-t_m (nm)	Composition (at. %)		
						[Mn]	[Si]	[N]
6	5	9	11	4.6×10^{16}	7.6	0.42	0.14	0.44
3	10	6	6.9	2.2×10^{16}	3.8	0.31	0.16	0.53
1.5	20	4.5	5.3	1.1×10^{15}	1.9	0.25	0.18	0.57
0.7	43	3.7	4.2	5.9×10^{16}	0.86	0.17	0.25	0.58
0.4	75	3.4	3.6	4.1×10^{15}	0.5	0.13	0.28	0.59
0.2	75	3.2	3.4	2.9×10^{15}	0.28	0.10	0.30	0.60
0.1	75	3.1	3.1	1.9×10^{15}	0.17	0.07	0.35	0.59

tected by RBS and NRA experiments (less than 5 at. %). Both, the reduced Mn density in RBS simulations and the absence of oxygen indicate that manganese nitridation occurs at the Mn-rich layers.

Previous works have related the oxygen content to the deposition method. These works are based on the tendency of Si_3N_4 to develop the corresponding oxynitride which can lead to strong modification of the physical properties. However, in contrast to deposition from Si_3N_4 ceramic targets, reactive sputtering from Si, as it has been done here, leads to lower oxygen content.[18,31]

B. Magnetic characterization

The magnetic characterization results of the Mn/Si_3N_4 samples are displayed in Fig. 3. Magnetization per Mn atom has been calculated by using the amount of Mn determined from the RBS measurements. Figure 3(a) shows the hysteresis loops recorded at RT and 5 K for selected samples with t_m ranging from 3.5 to 0.14 nm. In all cases, the diamagnetic contribution of the silicon substrate has been subtracted from the recorded data. For the $t_m=0.14$ nm sample, a high paramagneticlike component is observed at first glance. While this sample exhibits a very weak FM ordering, the RT magnetization of the $t_m=3.5$ nm sample indicates the existence of an average magnetic moment of $\sim0.4\mu_B$ per Mn atom. This value corresponds to about 110 emu/cm^3 at RT, being the highest saturation magnetization among the samples studied here. This sample shows a coercive field $H_C\sim60$ Oe at RT. Similar H_C values, ranging between 50 and 80 Oe, are found for the whole set of samples.

The origin of ferromagnetism in the Mn/Si_3N_4 system has been attributed to the presence of a distorted Mn_3N_2 FM phase with a T_C higher than 400 K, which seems to be favored by the Si_3N_4 tetrahedral structure.[17] In this work, ferromagnetism has been obtained for most of the prepared samples. The temperature dependence of magnetization $M(T)$ measured under an applied magnetic field of 100 Oe, can be seen in Fig. 3(b). An ordering temperature well above 400 K can be inferred for samples with $t_m\geq0.5$ nm. For samples with smaller t_m, although an enhancement of T_C could be evoked from the M-T curves, their smaller FM response together with the complexity of M versus T measurements over 400 K for thin film samples, make difficult to assert an increase of T_C. The evolution of the saturation magnetization (M_S) at RT versus the measured Mn layer thickness (t_m) for all the obtained FM samples is represented in Fig. 3(c). For small Mn layer thickness, M_S increases with t_m, exhibiting a maximum for a Mn layer thickness of the order of the Si_3N_4 one (~3.5 nm), while M_S decreases for further t_m increase. The importance of the Si_3N_4 layer thickness into the magnetic properties is also evidenced in the inset of Fig. 3(a), that shows the M(T) curves of several samples prepared with constant Mn layer thickness ($t_m=0.7$ nm), same number of repetitions ($n=43$) and different Si_3N_4 layer thickness, t_{sn} (ranging from 6.7 to about 1 nm).

Although it should be noted that smaller magnetization values are found for the samples prepared varying t_{sn} in comparison with the t_m variable series, it can be noticed that the highest FM signal within this variable t_{sn} series is obtained for the sample labeled as $[Mn(0.7\ nm)/Si_3N_4(1\ nm)]_{43}$. The fact that the $[Mn(3.5\ nm)/Si_3N_4(3.4\ nm)]_{10}$ sample exhibits

TABLE II. Description of selected samples, nominally named $[Mn(0.6\ nm)/Si_3N_4(t_{sn})]_{43}$: nominal Si_3N_4 thickness (t_{sn}), number of bilayers (n), nominal bilayer thickness (Λ), XRR-obtained bilayer thickness (XRR-Λ), XRR-obtained Si_3N_4 thickness (XRR-t_{sn}) and atomic composition, obtained from simulation of RBS and NRA.

Nominal t_{sn} (nm)	n	Nominal Λ (nm)	XRR-Λ (nm)	Mn-layer atomic density (at./cm^2)	XRR-t_{sn} (nm)	Composition (at. %)		
						[Mn]	[Si]	[N]
6	43	6.6	7.4	4.7×10^{15}	6.7	0.08	0.34	0.58
3	43	3.6	4.1	4.8×10^{15}	3.4	0.13	0.27	0.60
1.5	43	2.1	2.3	4.8×10^{15}	1.6	0.20	0.20	0.60
0.7	43	1.7	1.7	4.7×10^{15}	1.0	0.25	0.14	0.61

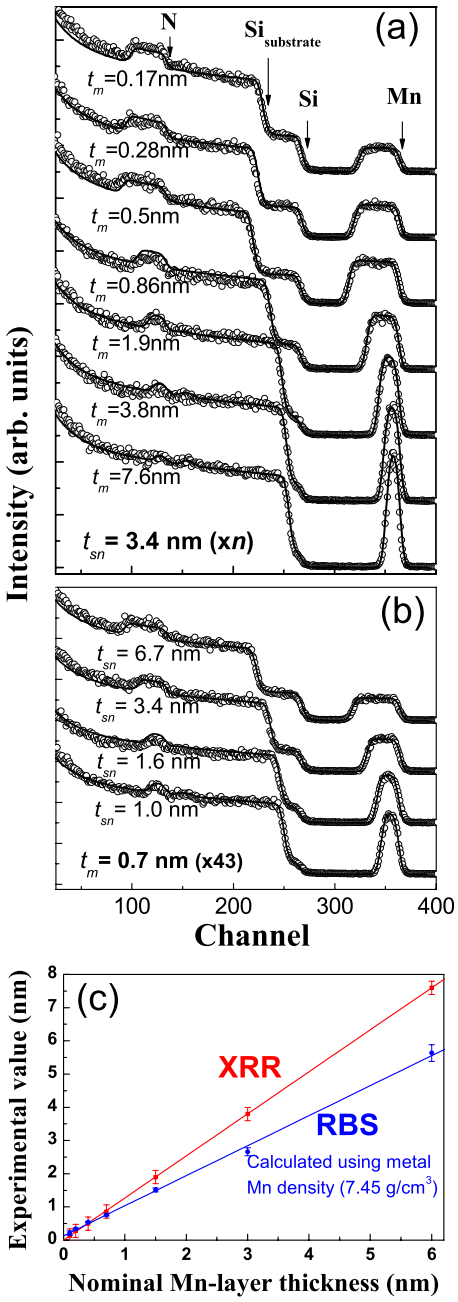

FIG. 2. (Color online) (a) RBS spectra taken at energy of incident ions of 2 MeV (dots) and their simulations (lines) of several Mn/Si_3N_4 samples with different Mn-layer thickness (t_m). (b) RBS spectra of several samples with different Si_3N_4-layer thickness (t_{sn}). All spectra have been vertically shifted for clearness. (c) Comparison between experimental Mn layer thickness values obtained from XRR and calculation from RBS.

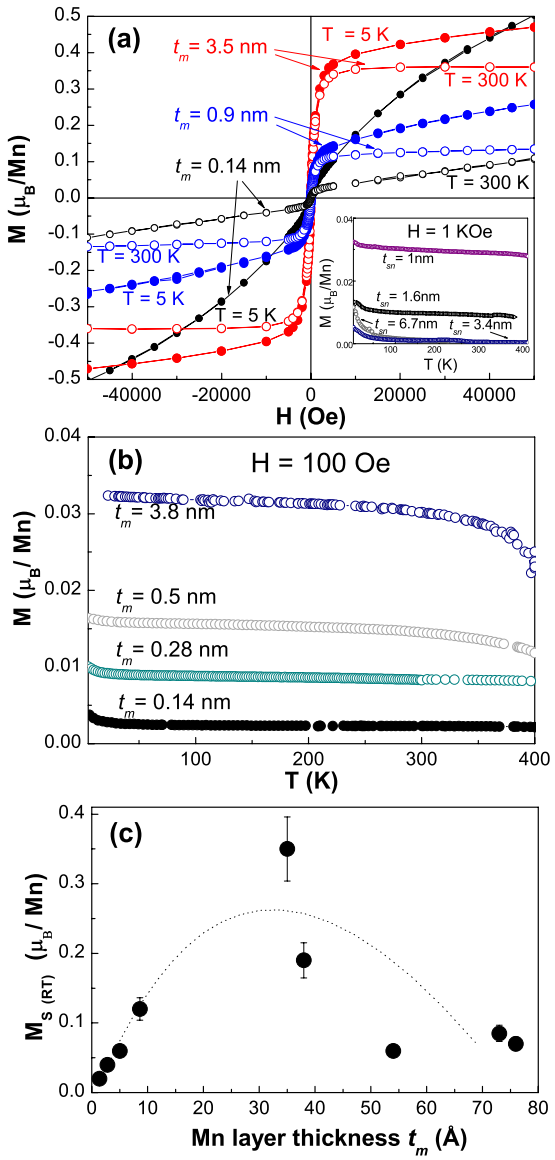

FIG. 3. (Color online) (a) Hysteresis loops of several samples measured at 5 K and RT. The inset shows the effect of modifying the Si_3N_4 layer thickness on the magnetization curves (H=1 kOe) for a Mn layer thickness constant (t_m=0.7 nm). (b) Magnetization vs temperature (H=100 Oe) for several samples with different Mn layer thickness (t_m). (c) Variation of the saturation magnetization at RT with the Mn layer thickness (t_m) for all the FM samples obtained. A dotted-line is included just as a guide to the eyes.

the highest M_S value points out that the FM alignment is favored when both, the manganese-rich and the silicon nitride layers have comparable thicknesses.

C. XPS and XAS

The above results suggest a relationship between the way in which the distorted Mn_3N_2 FM phase develops at the interface and the magnetic properties. For this reason we have undertaken a detailed study on the formation of such phase in this multilayer system.

In order to study the electronic properties of Mn-rich layers, we have performed an XPS study of two samples, the t_m=7.6 nm sample, representative of the thick Mn layer samples, and the t_m=0.5 nm one, where noncontinuous Mn is expected. Depth profiles were performed by removing thin layers of material with a calibrated sputtering gun operated with Ar+ ions of 1.4 eV kinetic energy. The photoemission spectra were collected after each sputtering sequence in order to follow the evolution of the electronic structure as a function of depth into the samples. The depth-profile Si, N, and Mn compositions of the t_m=7.6 nm sample are shown in Fig. 4. It can be observed that the depth-profile concentrations of the different elements are in rather good agreement with the layer period for the t_m=7.6 nm sample. As stated above, XPS spectra of the different elements present in the

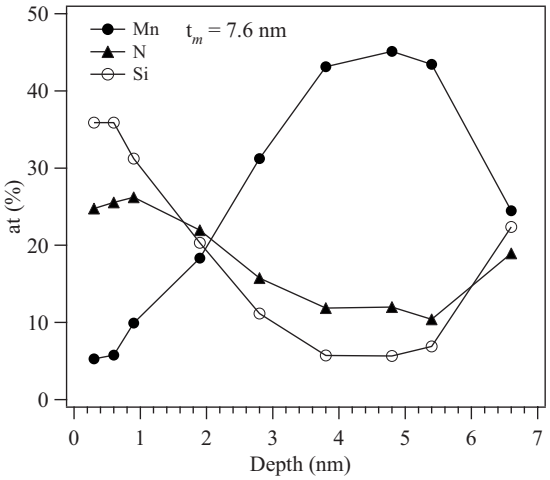

FIG. 4. XPS depth profile of the t_m=7.6 nm sample.

samples have been measured after each sequence of sputtering. In Fig. 5 we display the Mn 3*p* spectra of these two samples that were measured at the experimental point located at the depth of 5.4 nm (cf. Figure 4). For the case of t_m=0.5 nm sample, since Mn layers are very thin and embedded into Si_3N_4 layer, it is not possible to distinguish different Mn layers from the XPS signal and therefore, this

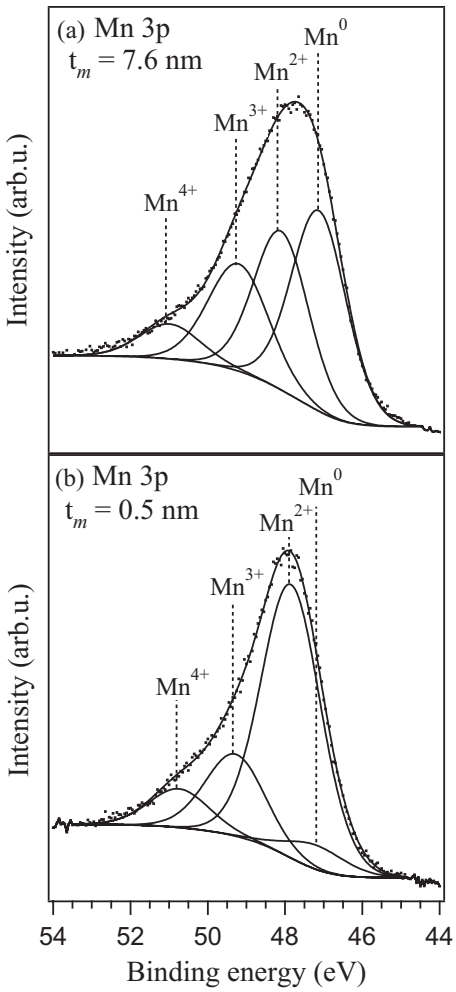

FIG. 5. Mn 3*p* XPS spectra of the t_m=7.6 nm and t_m=0.5 nm with the corresponding decomposition analysis into the different Mn valence states.

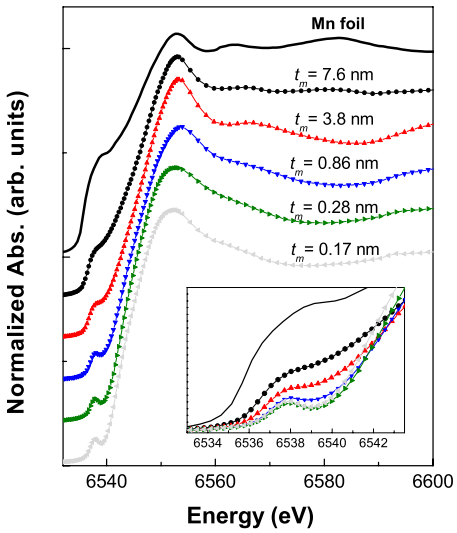

FIG. 6. (Color online) Mn *K*-edge XANES spectra of Mn/Si_3N_4 samples with different Mn layer thickness (t_m) values and a metallic Mn foil. Spectra have been vertically shifted for clearness. The inset shows a zoom of the prepeak region.

depth is not very significant. Anyway, it was chosen to be the same in both cases. The Fig. 5 also displays the corresponding peak decomposition into the different Mn valence states. Through the fitting analysis it clearly appeared that the samples exhibit different Mn valence states. For the t_m =7.6 nm sample, majority of metal and Mn^{2+} contributions has been obtained (about 40% Mn metal, 31% Mn^{2+}, 22% Mn^{3+}, and 7% Mn^{4+} are given from the fits, where an uncertainty between 5%–10% can be expected). Despite the small additional contribution from higher oxidized species, if we consider the majority species, the metallic Mn/Mn^{2+} ratio is about 4/3. For the t_m=0.5 nm sample, mostly Mn^{2+} contribution was deduced from the XPS analysis (about 6% Mn metal, 65% Mn^{2+}, 20% Mn^{3+}, and 9% Mn^{4+}). The extra Mn^{3+} and Mn^{4+} high valence contributions are approximately the same in both samples. However, the Mn metallic phase is drastically reduced in this former sample, being the Mn^{2+} valence state the dominant one. The obtained Mn average oxidation states are about +1.9 for the t_m=7.6 nm sample and +2.3 for the t_m=0.5 nm one.

Aimed at determining the Mn electronic state, the local structure of the Mn sites and the presence of Mn–N alloys, we have performed a combined XANES and EXAFS study of the $[Mn(t_m)/Si_3N_4(3.4\ nm)]_n$ and $[Mn(0.7\ nm)/Si_3N_4(t_{sn})]_{43}$ samples. The normalized Mn *K*-edge XANES spectra of representative samples are shown in Fig. 6. The threshold energy position evidences an average Mn oxidation state close to +2, in agreement with XPS results. Details of the prepeak region can be seen in the inset, showing an evolution of the prepeak intensity from the manganese foil reference to the samples with thinner Mn layer. As shown in Fig. 6, the shape and the main spectral features of the spectra change as t_m is varied. Therefore, we have studied the possible formation of a Mn–N alloy in the samples by comparing the experimental Mn *K*-edge XANES spectra and the results of theoretical simulations. It should be noted that despite the current

progress in XANES computation, several problems, as the treatment of the inelastic losses of the photoelectron, still remain as open problems.[32] Therefore we have started the computation on a reference material, metallic α-Mn, in order to fix the main parameters of the calculations. The first step of the calculations was deserved to determine the size of the cluster needed to reproduce all the spectral features present in the experimental XANES spectra. To this end we have performed the computation of the Mn *K*-edge XANES in the case of α-Mn (I-43m) by increasing progressively the number of atoms in the cluster. It should be noted that because Mn occupies four different crystallographic positions 2*a* (Mn1), 8*c* (Mn2), 24*f* (Mn3), and 24*g* (Mn4), XANES computations have to be performed for four different clusters in which the absorbing Mn atom lies at the different Mn_i sites, being the theoretical spectrum made up from the weighted sum of these contributions according the crystallographic statistical ratio. In this way, we have determined that the computations performed for clusters including contributions from neighboring atoms located within the first 7 Å around photoabsorbing Mn account for all the observed spectral features, and that further coordination shells do not contribute significantly to the XANES spectrum. We have also studied the effect of both the maximum angular momentum quantum number l_{max} and the overlapping factor imposed to the MT spheres to build up the potential[27] into reproducing the Mn *K*-edge XANES spectrum. We have found that the best reproduction of the experimental spectrum is obtained by using $l_{max}=4$ and a 1% overlapping factor to build up a 7 Å cluster. The results of these computations are shown in Fig. 7(a). The agreement between the computations and the experimental signal is noticeable as the calculations reproduce the steplike profile at the threshold (A), the main peak (B) and the two structures located at 28 (C) and 47 eV (D) above the edge. During the calculations we have tested the performance of the energy dependent HL and Dirac–Hara (DH) exchange and correlation (ECP) potentials. Moreover, we have also made computations by using only the real part of the HL ECP (hereafter, real HL) and, in addition, we have built a "complex" DH one by adding to it the imaginary part of the HL one. As shown in Fig. 7(a), the performances of the different EPC potentials are similar although in the case of the HL the calculated absorption maxima falling short of the observed ones. By contrast, computations performed by using the DH ECP show a better reproduction of the relative energy position among the peaks. This is evidenced by the reproduction of the main resonance D and the negative dip E located, respectively, at 47 and 62 eV above the edge. Moreover, the addition of the imaginary part of the HL potential improves the calculations yielding the use of the complex DH ECP the best reproduction of the intensity ratio among the different spectral features. It should be noted that the assessment of the quality of the theoretical computations is based on the correct reproduction of the shape and energy position of the different spectral features and of their relative energy separation and intensity ratio as well.

Possessing these results we have further performed the computation of the Mn *K*-edge spectrum in the case of both θ-MnN and η-Mn_3N_2. In the case of MnN, computations have been performed for a cluster containing 179 atoms that includes all the contributions from neighboring atoms located within the first 7.4 Å around the absorbing Mn atom. In the case of Mn_3N_2, Mn occupies two different crystallographic sites 2*a* (Mn1) and 4*e* (Mn2). Hence, XANES computations have been performed for two clusters in which the absorbing Mn atom lies at the different Mn1 and Mn2 sites. These clusters include the scattering contributions within the first 7.5 Å around the absorber and contain 153 and 150 atoms for Mn1 and Mn2, respectively. The Mn *K*-edge absorption of Mn_3N_2 has been calculated by adding the theoretical computations obtained for both clusters according to the crystallographic statistical ratio.

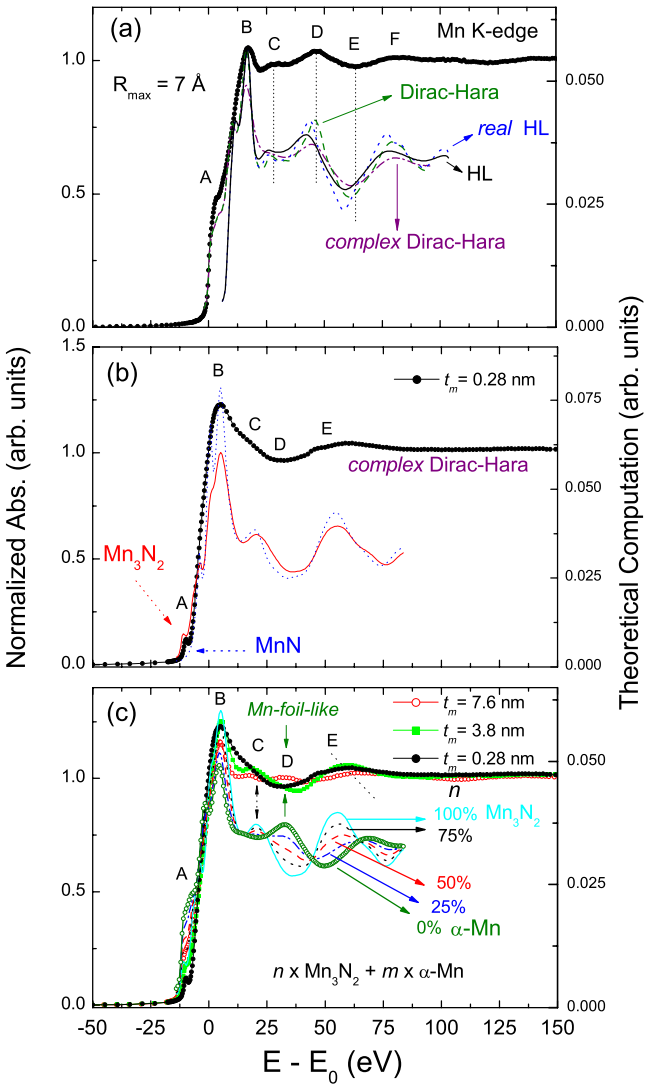

FIG. 7. (Color online) (a) Comparison between the Mn *K*-edge of a Mn metallic foil (●) and the theoretical spectra calculated on a 7 Å cluster by using $l_{max}=4$ and different ECP potentials: real HL (blue, dots), real DH (green, dashed line), complex HL (black, solid line) and complex DH (purple, dot-dashed). (b) Comparison between the experimental Mn *K*-edge XANES of the $t_m=0.28$ nm Mn sample (●) and the theoretical computation performed for both MnN (blue, dots) and Mn_3N_2 (red, solid line) by using the complex DH ECP potential. (c) Comparison between the experimental Mn *K*-edge XANES of the $t_m=0.28$ nm (black, ●), $t_m=3.8$ nm (green, □) and $t_m=7.6$ nm (red, ○) samples and the theoretical signals calculated as the weighted sum of the computed spectra for both Mn_3N_2 and α-Mn as a function of the Mn_3N_2 fraction *n*: 100% (cyan, solid line), 75% (black, dots), 50% (red, dashed), 25% (blue, dot-dashed) and 0% (green, ○).

The results of these computations are compared to the experimental spectrum of the t_m=0.28 nm sample in Fig. 7(b). The computed spectra show similar oscillations in the high energy region. However, their spectral profiles at the threshold region differ, especially concerning the pre-edge peak (A). This peak is experimentally observed and typically assigned to a noncentrosymmetric environment of the absorbing site, such as in tetrahedral coordination (T_d) symmetry. The theoretical simulation reproduces this peak for η-Mn_3N_2, while it is absent for MnN. These results suggesting the presence of η-Mn_3N_2 in our samples have been verified by studying the modification of the XANES spectra as a function of the thickness. Indeed, as the Mn thickness increases the η-Mn_3N_2 contribution should be hindered as the XANES would be made by the superposition of the XANES spectra of both η-Mn_3N_2 and bulk-Mn-like. This is shown in Fig. 7(c), where the XANES spectra of the samples with different Mn thickness (t_m) are compared to the theoretical spectra calculated as the weighted addition of the computed spectra for η-Mn_3N_2 and α-Mn in the form: $n \times Mn_3N_2 + m \times \alpha$-Mn. As shown in the figure, the modification of the Mn thickness strongly changes the spectral profile in the high energy region. For example, in the case of the sample with the small Mn thickness (t_m=0.28 nm) the spectrum shows a negative dip (D) at ~33 eV above the edge. As the Mn thickness increases, samples t_m=3.8 nm and t_m=7.6 nm, this spectral feature evolves up to yield a positive resonance. This is exactly the situation obtained in the theoretical simulation of Fig. 7(c): whereas the Mn_3N_2 dominates the spectrum, feature D remains negative but, however, as the contribution of bulk Mn increases, the sign of this contribution is reversed. Similar analysis can be followed for the energy position of the main resonance E at ~57 eV above the edge. Experimentally, this feature is shifted toward higher energies as the Mn thickness increases in the samples, in identical manner to the behavior of the theoretical signal constructed by varying the weight of the η-Mn_3N_2 and α-Mn contribution to the XANES spectra. The obtained evolution agrees with the Mn_3N_2:Mn ratio obtained by XPS.

Therefore, the *ab initio* calculations have evidenced the presence of both metallic and Mn_3N_2 phase (with Mn T_d symmetry) in sample t_m=7.6 nm, while no sign of Mn metallic phase appears in the t_m=0.28 nm spectrum, which presents just nitride contribution. The fact that increasing the Mn-layer thickness leads to a reduction of the relative contribution of η-Mn_3N_2 compared to the bulklike Mn indicates that the Mn nitride formation in the sputtered Mn layer is related to the Si_3N_4 interfaces, leading, for thin enough Mn-rich layers, to all the deposited Mn turned into manganese nitride.

Further confirmation of these results has been obtained by studying the Mn local environment from the analysis of the EXAFS part of the spectra. Figure 8 shows the evolution of the FT magnitude of the EXAFS signal at the Mn *K*-edge along the series with t_m variable and a Mn metal foil, given for comparison. At first glance, clear differences between the FT magnitude of the t_m=7.6 nm sample and the others, as well as the extinction of the FT second peak for small t_m values, are observed.

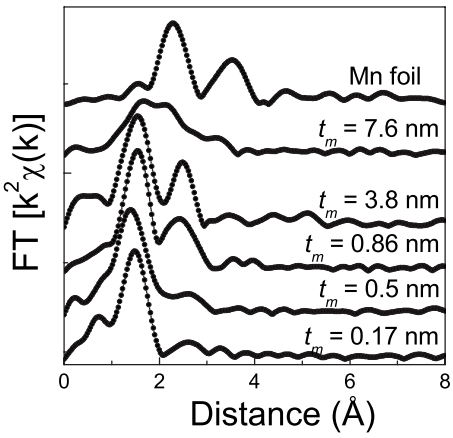

FIG. 8. Experimental EXAFS FT of some representative $[Mn(t_m)/Si_3N_4(3.4\ nm)]_n$ samples and a Mn metal foil.

The comparison between experimental data and simulations is shown in Fig. 9, and the obtained results are summarized in Table III. Analysis shows a complex situation that can be explained as follows. A contribution around 2.05 Å corresponding to Mn–N distance is present for all the sample series and besides, samples with t_m higher than 0.5 nm present a second Mn–Mn near 3 Å. Those distances agree with Mn_3N_2 compounds with slightly compressed distances.[9] Additionally, a small Mn–Si contribution at about 3.1 Å has been found for t_m=0.86 nm and t_m=3.8 nm samples, what can be assigned to the link between the Mn_3N_2 and Si_3N_4 phases. Finally, the Mn–Mn distance found at 2.67 Å in sample t_m=7.6 nm is in agreement with distances in metallic

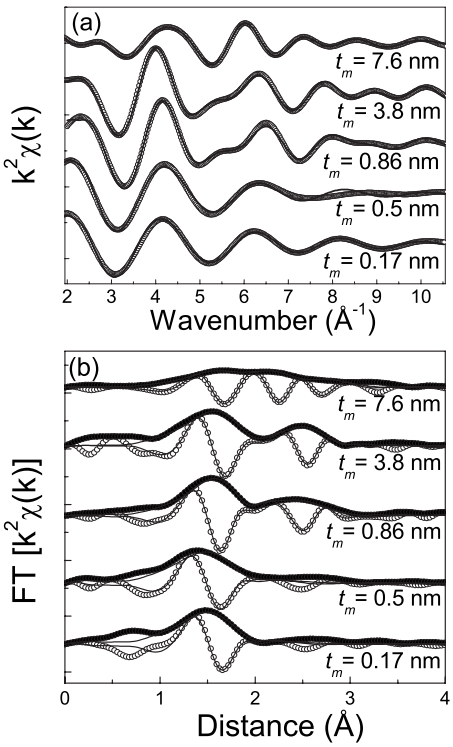

FIG. 9. (a) *k*-space comparison between the filtered EXAFS signals (dots) and simulations (lines) at the Mn *K*-edge of samples with different Mn layer thickness (t_m). (b) FT of the (a) plotted signals; modulus and imaginary parts have been presented for dual comparison with calculated contributions (lines).

TABLE III. EXAFS results summary: atomic distance (R), number of neighbors (N) and Debye–Waller factor (σ^2).

Sample (nm)	Pair	R (Å)	N	σ^2 ($\times 10^{-3}$ Å^2)
$[Mn(t_m)/Si_3N_4(3.4)]_n$				
t_m=7.6	Mn–N	2.03±0.02	2.4±1	5±1
	Mn–Mn	2.67±0.02	4.2±1	25±1
	Mn–Mn	2.98±0.02	6.0±1	29±1
t_m=3.8	Mn–N	2.06±0.02	3.1±1	9±1
	Mn–Mn	3.06±0.02	3.4±1	17±1
	Mn–Si	3.12±0.02	2.3±1	7±1
t_m=0.86	Mn–N	2.04±0.02	2.6±1	7±1
	Mn–Mn	2.98±0.02	2.8±1	7±1
	Mn–Si	3.10±0.02	1.1±1	9±1
t_m=0.5	Mn–N	2.02±0.02	2.9±1	12±1
t_m=0.28	Mn–N	2.06±0.02	3.1±1	22±1
t_m=0.17	Mn–N	2.04±0.02	2.7±1	8±1
$[Mn(0.7)/Si_3N_4(t_{sn})]_{43}$				
t_{sn}=6.7	Mn–N	2.04±0.02	2.9±1	10±1
t_{sn}=1.0	Mn–N	2.03±0.02	3.2±1	6±1

Mn. The expected small size of Mn_3N_2 clusters explains the disappearance of the FT second peak for $t_m \leq 0.5$ nm and does not allow to obtain Mn–Mn and Mn–Si distances for these samples. In the case of the t_m=7.6 nm sample, EXAFS results are in agreement with previous XANES conclusions. For this sample, significant presence of metallic Mn (with Mn–Mn distances widely spread around 2.7 Å) is found; this additional phase as well as the small number of layers make very hard to obtain the minority Mn–Si contribution. At this point, it is important to note that the observation of this Mn–Si EXAFS distance supports the fact that Mn_3N_2 phase is formed at the interface between the Mn and Si_3N_4 layers, suggesting that the Si_3N_4 has a definitive influence in the development of a strained Mn_3N_2 phase. Within the error in the neighbor number determination, the Mn metal/Mn_3N_2 ratio obtained by EXAFS is compatible with the one extracted by both XPS and XANES data (4:3). By contrast, no appreciable Mn metal contribution is obtained from the EXAFS analysis of the t_m=3.8 nm sample. In comparison with the other samples, slightly higher Mn–Mn distances (3.06 Å) are found in the Mn_3N_2 phase of the t_m=3.8 nm sample, being one of the most FM ones. Results from EXAFS simulations of samples with different Si_3N_4 layer thickness (Fig. 10) are included in Table III. As expected, similar Mn–N distances are obtained when varying t_{sn}. It can be observed that the change in the atomic environment when varying t_{sn} is smaller than the resulting when modifying t_m, where larger magnetization values were found. Just very small differences are detected by EXAFS for the samples with different t_{sn} values.

D. Concluding remarks

Regarding all the obtained results, the evolution of M_S within the multilayer series can be qualitatively understood. For samples with Mn-rich layers smaller than 0.86 nm, mostly Mn^{2+} contribution was obtained from XPS, being this

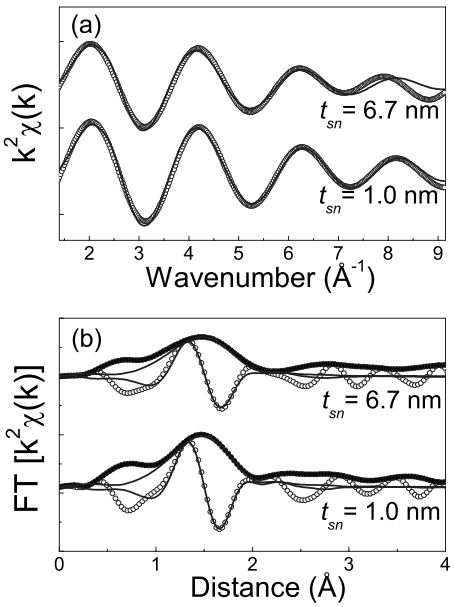

FIG. 10. (a) k-space comparison between the filtered EXAFS signal (dots) and simulations (lines) at the Mn K-edge of samples with different Si_3N_4 layer thickness (t_{sn}). (b) FT of the (a) plotted signals; modulus and imaginary parts have been presented for dual comparison with calculated contributions (lines).

Mn^{2+} average oxidation state corroborated by XANES measurements at the Mn K-edge. The Mn_3N_2 phase formation has been verified by EXAFS and XANES simulations. EXAFS results have shown the disappearance of the second neighbor shell for these samples, indicating the presence of Mn_3N_2 clusters of small size. The decrease in the magnetization for these samples is explained in terms of the superparamagnetic size limit, which becomes important for particle sizes around 1 nm. Looking at the hysteresis loops at low temperature [cf. Fig. 3(a)] it can be noticed how the superparamagnetic component becomes significant as t_m is reduced.

On the other hand, for large Mn-rich layer thickness samples, major contributions of both, metallic Mn and Mn^{2+}, have been found by XPS. The metallic Mn presence as well as the Mn_3N_2 formation favored by the Si_3N_4 presence, have been corroborated by the EXAFS results and XANES calculations. In this case, the reduction of M_S is understood through the formation of the metallic Mn phase, that reduces the specific magnetization per Mn atom.

A scheme of both cases is shown in Fig. 11. It should be noticed that minor contributions from possible additional phases (MnN or Mn_4N, for instance) can complicate this image. However, it is important to remark that the origin of ferromagnetism in this system was previously ascribed to a Mn d^5 contribution (Mn^{2+}) by x-ray magnetic circular dichroism (XMCD) experiments. These investigations have allowed to discard FM due to Mn metallic clusters, ternary phases such as $MnSiN_2$,[33] FM due to Mn^{2+} substitution into the Si_3N_4 matrix or formation of manganese nitride such as Mn_4N, Mn_2N, or Mn_5N_2 phases.

In order to estimate the reduction of the M_S due to the presence of metallic Mn, we have calculated the effective saturation magnetization at RT of sample t_m=7.6 nm by nor-

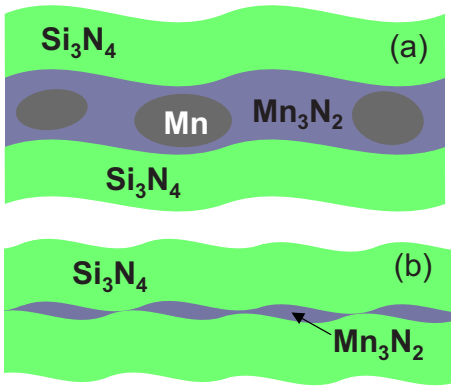

FIG. 11. (Color online) Simplified structural image of the multilayer samples (a) with larger Mn layer thickness (t_m), where Mn metal and Mn_3N_2 phases coexist, and (b) with $t_m < 0.86$ nm, where noncontinuous Mn_3N_2 layers are formed.

malizing only to the Mn coming from Mn_3N_2 (about 30% from XPS data), instead of all the Mn atoms [previously considered in Fig. 3(c)]. This leads to about $0.23\mu_B$ per Mn atom at RT, being closer to the maximum value of M_S within the series, about $0.35\mu_B$ per Mn atom. Another factor, such as small differences in the lattice parameters (Mn–Mn distances larger than 3 Å were found for the $t_m = 3.8$ nm sample) seems to be directly related to variations in the FM order established in the Mn_3N_2 distorted phase. The role of the Si_3N_4 layer thickness in the ferromagnetism has been also evidenced in the $[Mn(0.7\ \text{nm})/Si_3N_4(t_{sn})]_{43}$ series, even if higher M_S values and stronger variation were obtained when varying the Mn layer thickness (t_m). The stabilization of the FM Mn_3N_2 distorted phase results favored when both, the manganese-rich and the silicon nitride layers are comparable in thickness, where slightly larger Mn–Mn distances were found. This point is consistent with the fact of finding Mn–Si EXAFS contribution in samples with intermediate t_m, what evidences a clear relationship between the Mn_3N_2 distorted phase and the surrounded Si_3N_4 for these similar thicknesses, where the imprinted stresses seem to promote the stabilization of the Mn_3N_2 distorted phase.

IV. CONCLUSIONS

In conclusion, FM order has been regularly obtained in Mn/Si_3N_4 multilayered samples with different $Mn:Si_3N_4$ relative ratios. A variation of the magnetic properties has been obtained by modifying the Mn and the Si_3N_4 layer thickness. The magnetic behavior of these films has been related to the stabilization of a noncentrosymmetric Mn_3N_2 phase with slightly shorter Mn–N distances induced by the Si_3N_4 presence.

For samples with larger Mn-rich layer thickness, the Mn_3N_2 FM phase coexists with metal Mn phase, that reduces the total magnetization per Mn atom. By contrast, for very small Mn-rich layer thickness ($t_m < 0.86$ nm), small Mn_3N_2 clusters are formed, decreasing the magnetization as the cluster size diminishes due to the superparamagnetic size limit. The best condition to stabilize the FM ordering in this system occurs when the manganese-rich and silicon nitride layers are continuous and their thicknesses are comparable and close to 3.5 nm, where slightly larger Mn–Mn distances were found. Several factors as, small differences in the atomic distances, formation of possible additional phases or the inherent instability of the formed phase can lead to more complicated magnetic behaviors.

ACKNOWLEDGMENTS

This work has been supported under Contract Nos. MAT2006-01004, MAT2008-06542-C04-01, MAT2008-06765-C02-02, S-0505/MAT/0194, Consolider 2010_26400, and Nanoselect CSD2007-00041. Support from ESRF staff during the experiments is greatly acknowledged, especially to Dr. Fabrizio Bardelli at GILDA.

[1] H. Yang, H. Al-Britten, R. Smith, J. A. Borchers, R. L. Cappelletti, and M. D. Vaudin, Appl. Phys. Lett. **78**, 3860 (2001).
[2] S. Granville, B. J. Ruck, F. Budde, A. Koo, J. E. Downes, H. J. Trodahl, A. Bittar, N. Strickland, G. V. M. Williams, W. R. L. Lambrecht, T. Learmonth, K. E. Smith, V. J. Kennedy, A. Markwitz, and T. Schmitt, Phys. Rev. B **72**, 205127 (2005).
[3] M. Chiba and S. Naito, e-J. Surf. Sci. Nanotechnol. **6**, 115 (2008).
[4] J. A. Chan, J. Z. liu, H. Raebiger, S. Lany, and A. Zunger, Phys. Rev. B **78**, 184109 (2008).
[5] B. K. Rao and P. Jena, Phys. Rev. Lett. **89**, 185504 (2002).
[6] M. Marques, L. K. Teles, L. M. R. Scolfaro, J. Furthmüller, F. Bechstedt, and L. G. Ferreira, Appl. Phys. Lett. **86**, 164105 (2005).
[7] W. R. L. Lambrecht, M. Prikhodko, and M. S. Miao, Phys. Rev. B **68**, 174411 (2003).
[8] H. Yang, H. Al-Britten, E. Trifan, D. C. Ingram, and A. R. Smith, J. Appl. Phys. **91**, 1053 (2002).
[9] M. Hasegawa and T. Yagi, J. Alloys Compd. **403**, 131 (2005).
[10] K. Suzuki, T. Kaneko, H. Yoshida, Y. Obi, H. Fujimori, and H. Morita, J. Alloys Compd. **306**, 66 (2000).
[11] A. F. Guillerment and G. Grimvall, Phys. Rev. B **40**, 10582 (1989).
[12] H.-M. Hong, Y.-J. Kang, J. Kang, E.-C. Lee, Y.-H. Kim, and K. J. Chang, Phys. Rev. B **72**, 144408 (2005).
[13] M. Marques, L. M. R. Scolfaro, L. K. Teles, J. Furthmüller, and F. Bechstedt, Appl. Phys. Lett. **88**, 022507 (2006).
[14] S. Nakagawa and M. Naoe, J. Appl. Phys. **75**, 6568 (1994).
[15] F. Munakata, K. Matsuo, K. Furuya, Y. Akimune, J. Ye, and I. Ishikawa, Appl. Phys. Lett. **74**, 3498 (1999).
[16] A. R. Zanatta and L. A. O. Nunes, Appl. Phys. Lett. **72**, 3127 (1998).
[17] E. Céspedes, Y. Huttel, L. Martínez, A. de Andrés, J. Chaboy, M. Vila, N. D. Telling, G. van der Laan, and C. Prieto, Appl. Phys. Lett. **93**, 252506 (2008).
[18] M. Vila, D. Cáceres, and C. Prieto, J. Appl. Phys. **94**, 7868 (2003).
[19] K. V. Klementiev, VIPER for WINDOWS, freeware: http://www.desy.de/~klmn/viper.html; J. Phys. D **34**, 209 (2001).
[20] S. I. Zabinsky and J. J. Rehr, Phys. Rev. B **52**, 2995 (1995).
[21] C. R. Natoli and M. Benfatto (unpublished).
[22] P. A. Lee and J. B. Pendry, Phys. Rev. B **11**, 2795 (1975).
[23] C. R. Natoli and M. Benfatto, J. Phys. Colloq. **47**, C8 (1986).
[24] See, for example, J. Chaboy and S. Quartieri, Phys. Rev. B **52**, 6349 (1995) (and references therein).
[25] C. R. Natoli, M. Benfatto, S. Della Longa, and K. Hatada, J. Synchrotron Radiat. **10**, 26 (2003).
[26] L. F. Mattheiss, Phys. Rev. **133**, A1399 (1964); L. F. Mattheiss, *ibid.* **134**, A970 (1964).
[27] J. G. Norman, Mol. Phys. **81**, 1191 (1974).
[28] J. P. Desclaux, Comput. Phys. Commun. **9**, 31 (1975).
[29] P. A. Lee and G. Beni, Phys. Rev. B **15**, 2862 (1977).
[30] M. O. Krause and J. H. Oliver, J. Phys. Chem. Ref. Data **8**, 329 (1979).
[31] M. Vila, E. Román, and C. Prieto, J. Appl. Phys. **97**, 113710 (2005).
[32] J. Chaboy, J. Synchrotron Radiat. **16**, 533 (2009).
[33] S. Esmaeilzadeh, U. Hålenius, and M. Valldor, Chem. Mater. **18**, 2713 (2006).